CRACD, a gatekeeper restricting proliferation, heterogeneity, and immune evasion of small cell lung cancer

Shengzhe Zhang,[1,†] Kee-Beom Kim,[2,3†] Yuanjian Huang,[1†] Dong-Wook Kim,[2] Bongjun Kim,[1] Kyung-Pil Ko,[1] Gengyi Zou,[1] Jie Zhang,[1] Sohee Jun,[1] Nicole A. Kirk,[2] Ye Eun Hwang,[2] Young Ho Ban,[4] Joseph M. Chan,[5] Charles M. Rudin,[5] Kwon-Sik Park,[2,‡] Jae-Il Park[1,6,7,‡]

[1]Department of Experimental Radiation Oncology, Division of Radiation Oncology, The University of Texas MD Anderson Cancer Center, Houston, TX 77030, USA

[2]Department of Microbiology, Immunology, and Cancer Biology, University of Virginia School of Medicine, Charlottesville, VA 22908, USA

[3]BK21 FOUR KNU Creative BioResearch Group, School of Life Sciences, Kyungpook National University, Daegu, 41566, Republic of Korea

[4]Hamatovascular Biology Center, Robert M. Berne Cardiovascular Research Center, University of Virginia School of Medicine, Charlottesville, VA 22908, USA

[5]Department of Medicine, Thoracic Oncology Service, Memorial Sloan Kettering Cancer Center, New York, NY 10065, USA

[6]Graduate School of Biomedical Sciences, The University of Texas MD Anderson Cancer Center, Houston, TX 77030, USA

[7]Program in Genetics and Epigenetics, The University of Texas MD Anderson Cancer Center, Houston, TX 77030, USA

[†]These authors contributed equally.

[‡]Correspondence: Kwon-Sik Park (kp5an@virginia.edu) and Jae-Il Park (jaeil@mdanderson.org)

Tel: 713-792-3659; Fax: 713-794-5369

Author Contributions: S.Z., K.-B.K., Y.H., K.-S.P., and J.-I.P. conceived and designed the experiments. S.Z., K.-B.K., Y.H., D.-W.K., B.K., Y.H.B., N.A.K., Y.E.H., G.Z., J.Z., and S.J. performed the experiments. S.Z., K.-B.K., Y.H., J.M.C., C.M.R., K.-S.P., and J.-I.P. analyzed the data. J.M.C. and C.M.R. provided the sequencing files and technical support for scRNA-seq analyses. S.Z., K.-S.P., and J.-I.P. wrote the manuscript.

Competing Interest Statement: The authors declare that they have no conflict of competing interests.

Keywords: CRACD, KIAA1211, small cell lung cancer, immune evasion, EZH2

Abstract

Small cell lung carcinoma (SCLC) is a lethal neuroendocrine type of lung cancer with limited therapeutic options. Despite recent advances in cancer immunotherapy, the efficacy of immunotherapy is limited to a subset of patients with SCLC. However, the mechanisms responsible for refractoriness to immunotherapy remain elusive. *CRACD* (capping protein inhibiting regulator of actin dynamics; *KIAA1211/CRAD*) is frequently mutated and transcriptionally downregulated in SCLC. Here we show that *Cracd* knockout (KO) enhances transformation of preneoplastic neuroendocrine cells and significantly accelerates SCLC development initiated by loss of *Rb1*, *Trp53*, and *Rbl2* in the lung epithelium of mice. *Cracd* KO increases tumor cell heterogeneity in SCLC tumors. Notably, the *Cracd*-deficient SCLC tumors display exclusion of $CD8^+$ T cells, which coincides with epigenetic suppression of the MHC-I pathway. Single-cell transcriptomic analysis identifies SCLC patient tumors with concomitant inactivation of CRACD and impairment of tumor antigen presentation. These findings define CRACD as a novel tumor suppressor that regulates the proliferation and immune recognition of SCLC cells, providing new insight into the mechanisms by which SCLC evades immune surveillance.

Significance statement

Although cancer immunotherapy shows promising outcomes, immunotherapy resistance is a major hurdle to overcome. Small cell lung cancer (SCLC) is a lethal neuroendocrine type of lung cancer with limited therapeutic options. We herein investigated role of the *CRACD* gene, which is frequently inactivated in SCLC. *Cracd* knockout (KO) significantly accelerated SCLC development in a mouse model. Strikingly, *Cracd* KO SCLC tumors displayed the complete loss of $CD8^+$ T cells via the epigenetic suppression of the MHC-I pathway. Furthermore, single-cell transcriptomics stratified SCLC patients by concurrent features: CRACD inactivation and tumor antigen presentation impairment. This study identifies CRACD as a tumor suppressor that restricts the proliferation and immune recognition of SCLC cells, providing novel insight into how SCLC evades immune surveillance.

Introduction

SCLC accounts for 13% of all lung cancers, and remains a particularly lethal disease, with a 5-year survival rate of 7%. It is estimated to cause approximately 30,000 patient deaths annually in the United States (Byers and Rudin, 2015; Howlader et al., 2019). Major contributing factors to the high mortality rate of SCLC patients include the high prevalence of metastasis at the time of diagnosis, which limits therapeutic options, and nearly universal disease relapse associated with resistance to further therapies (Bunn Jr et al., 2016; Gazdar et al., 2017). Notably, immune checkpoint blockade (ICB) approaches designed to target tumors expressing neoantigens are effective in only ~13% of patients with SCLC—a small subset, given that the high mutation burden of SCLC tumors should be sufficient to trigger a robust immune response from cytotoxic T lymphocytes (Iams et al., 2020; Pakkala and Owonikoko, 2018; Ragavan and Das, 2020).

While it remains unclear what underlies the refractoriness of SCLC to ICB and how to stratify patient tumors by the degree of response to ICB, recent studies have explored emerging molecular subtypes of SCLC tumors, classified based on the actions of key lineage transcription factors (ASCL1, NEUROD1, and POU2F3) and inflammation (Chan et al., 2021; Gay et al., 2021; Ireland et al., 2020; Rudin et al., 2019). However, the current classification system has not been robust enough to reliably predict immunotherapy response. Therefore, understanding how SCLC cells evade immune surveillance and become resistant to immunotherapy is imperative to improve the durability of ICB in responding patients, and to inform strategies to increase the fraction of patients benefitting from ICB.

We recently discovered a tumor suppressor gene called *CRACD* (Jung et al., 2018). CRACD is ubiquitously expressed in epithelial cells and binds to and inhibits capping proteins (CAPZA and CAPZB), which are negative regulators of actin polymerization (Jung et al., 2018). CRACD promotes actin polymerization, which is crucial for maintaining the cadherin-catenin-actin complex of epithelial cells. *CRACD* is recurrently mutated or transcriptionally downregulated in cancer cells, which results in reduction of filamentous actin (F-actin) and disruption of the cadherin-catenin-actin complex (Jung et al., 2018). These alterations cause loss of epithelial cell integrity and decrease the cytoplasm-to-nucleus volume ratio; cells become “small”. A pathological consequence of these alterations is evident in the intestines, where CRACD inactivation hyperactivates WNT signaling via β-catenin release from the cadherin-catenin-actin complex and accelerates intestinal tumorigenesis (Jung et al., 2018).

CRACD is also frequently genetically or epigenetically inactivated in SCLC, which led us to hypothesize that CRACD plays a tumor suppressor role in SCLC tumorigenesis. To test the hypothesis, we interrogated the impact of CRACD loss on SCLC development using preneoplastic cells and

genetically engineered mouse models (GEMMs) and through immune cell profiling and single-cell transcriptomic analysis of human SCLC tumors. Our findings nominate CRACD as a new tumor suppressor of SCLC and implicate CRACD loss as a driver of both intratumoral heterogeneity and immune evasion in SCLC.

Results

CRACD inactivation accelerates SCLC tumorigenesis

CRACD is mutated in 11-16% of SCLC patient tumors and SCLC cell lines, ranking in frequency after *RB1* and *TP53* but more frequently than *RBL2*, *CREBBP,* and *EP300* among validated tumor suppressor genes (SI Appendix, Fig. S1A-C, S2)(George et al., 2015; Jia et al., 2018; Jung et al., 2018; Ng et al., 2020; Peifer et al., 2012). CRACD expression was also lower in SCLC tumors than in healthy lung tissue samples (SI Appendix, Fig. S1D). These data led to the hypothesis that CRACD loss-of-function plays a role in SCLC tumorigenesis. To test this hypothesis, we determined whether *Cracd* knockout (KO) promotes the transformation of preneoplastic precursor cells of SCLC (preSCs). The preSCs were derived from early-stage neuroendocrine (NE) lesions developed in an *Rb1/Trp53*-mutant mouse model of SCLC and upon an oncogenic event, such as *L-Myc* amplification or *Crebbp*/*Ep300* loss progress to an invasive and fully malignant tumor (Jia et al., 2018; Kim et al., 2018; Kim et al., 2016). Utilizing the CRISPR/Cas9-mediated gene editing strategy to generate *Cracd* KO mice as previously described (Jung et al., 2018), we targeted exon 2 of *Cracd* in preSCs. *Cracd* KO preSCs readily transformed into aggregates and spheres that are typical of SCLC cells in culture and formed subcutaneous tumors in an allograft model significantly faster than did control preSCs (Fig. 1A-E, SI Appendix, Fig. S3). We also studied a GEMM in which *Rb1*$^{fl/fl}$, *Trp53*$^{fl/fl}$, and *Rbl2*$^{fl/fl}$ alleles (RPR2) were conditionally deleted on the background of *Cracd* wild-type (WT) alleles or germline *Cracd* KO (*Cracd*, *Rb1*, *Trp53*, and *Rbl2* quadruple KO [CRPR2]) (Gazdar et al., 2015; Schaffer et al., 2010). CRPR2 mice showed marked increases in tumor burden and number and mitotic index of SCLC tumors compared to those of RPR2 mice (Fig. 1F-K), suggesting that *Cracd* KO accelerates SCLC tumor development *in vivo*. These results indicate that CRACD plays a tumor suppressor role in SCLC development.

Cracd KO increases tumor cell phenotypic diversity

To explore the mechanisms by which CRACD loss accelerates SCLC tumorigenesis, we performed single-cell RNA-sequencing (scRNA-seq) of SCLC tumors isolated from the lung tissues of RPR2 and CRPR2 mice (SI Appendix, Fig. S4A). Two datasets (RPR2 and CRPR2) were integrated and annotated for each cell type (Fig. 2A, B, SI Appendix, Fig. S4). Epithelial tumor cell clusters were selected for further unsupervised sub-clustering (Fig. 2B, SI Appendix, Table S3). While 13 different cell clusters (clusters 2 and 4-15) were found in RPR2 tumors, 15 types of cell clusters (clusters 1-15) were identified in CRPR2 tumors (Fig. 2C). Overall, clusters 4-15 showed relatively higher expression of NE markers (*Ascl1*, *Calca*, and *Chga*) than clusters 1-3. Clusters 8-10 and 12 were enriched with cell proliferation markers (*Pcna*, *Pclaf*, and *Mki67*) (Fig. 2C). Relative to RPR2 tumors, CRPR2 tumors showed an

increased ratio of cell clusters 4, 6, and 7. Conversely, cluster 8 was markedly reduced in CRPR2 tumors. In addition, three cell clusters (1, 3, and 14) were almost exclusively observed in CRPR2 tumors (Fig. 2C, D).

Since *Cracd* KO affects the diversity of cell phenotypes seen in CRPR2 tumors, we explored whether it might affect tumor cell plasticity by inferring cell lineage trajectories using the RNA velocity algorithm (Bergen et al., 2020). The analysis using the scVelo package (Bergen et al., 2020) failed to identify significant differences in cell lineage trajectories between RPR2 and CRPR2 tumors (SI Appendix, Fig. S4A). However, a computational method that predicts cell fate transitions based on differential geometry using the Dynamo algorithm (Qiu et al., 2022) suggested that CRPR2 tumors exhibited a more complex pattern of cell lineage trajectories than did RPR2 tumors (*SI Appendix,* Fig. S5B, C, SI Appendix, Movie S1). Partition-based graph abstraction analysis further supported that CRACD loss increased phenotypic cell diversity (SI Appendix, Fig. S5C). We next assessed the effect of *Cracd* KO on cell de-differentiation using the CytoTRACE algorithm, which infers cell state (differentiation vs. de-*differentiation*) (Gulati et al., 2020). Most cell clusters of CRPR2 tumors showed relatively higher cell de-differentiation potential, i.e., less differentiation than did those of RPR2 tumors (Fig. 2E, F). The scRNA-seq analysis from the allograft tumors derived from *Cracd* WT and KO preSCs also predicted that *Cracd* KO altered cell lineage trajectories (SI Appendix, Fig. S6, S7, SI Appendix, Table S4, Movie S1).

To understand how CRACD loss *might* enhance tumor cell diversity, we identified key transcriptional circuits activated in cell clusters of CRPR2. A comparative geneset enrichment assay (GSEA) showed that compared to RPR2, the genesets of distinct cell clusters of CRPR2 were associated with activation of the epithelial-mesenchymal transition, hypoxia, MYC, and E2F pathways (Fig. 2G, H, and SI Appendix, Fig. S8). It is noteworthy that the cell clusters 1 and 2 in CRPR2 tumors were enriched with the SCLC genesets (SI Appendix, Fig. S8), reiterating the relevance of CRACD inactivation to human SCLC. Recent studies classified SCLC into four major subtypes (*ASCL1*, *NEUROD1*, *POU2F3*, and *YAP1*) (Ireland et al., 2020; Rudin et al., 2019). Compared to RPR2, *Cracd* KO tumors (CRPR2) were enriched in *Ascl1* and *Calca* expression, resembling the transcriptional signature of the ASCL1-subtype of SCLC (Fig. 2I).

Immune landscape remodeling of SCLC by *Cracd* KO

Given that immune cells play crucial roles in tumorigenesis by creating a tumor-favorable environment or killing tumor cells (Anderson and Simon, 2020; Bejarano et al., 2021), we next examined the impact of CRACD loss on the tumor microenvironment. Using scRNA-seq, we profiled immune cells in RPR2 and CRPR2 tumors that developed in the GEMMs (Fig. 3A-C, SI Appendix, Fig. S9). CRPR2 tumors harbored strikingly fewer $CD8^+$ T cells (6.86% [170 of 2477 cells]) than did RPR2 tumors (65.06%

[3484 of 5355 cells]) while showing a slightly higher ratio of naïve T cells to total cell numbers (26.52% [657 of 2477 cells] versus 20.24% [1084 of 5355 cells]) (Fig. 3C-E), which was also confirmed by immunostaining for $CD8^+$ T cells (Fig. 3F, G). Of note, the number of whole T cells and apoptotic cells remained similar between RPR2 and CRPR2 tumors (SI Appendix, Fig. S10). In addition, the expression of T cell exhaustion markers (*Pd-1* and *Pd-l1/2*) was not affected by *Cracd* KO in CRPR2 tumors compared to in RPR2 tumors (SI Appendix, Fig. S11A, B). Moreover, compared to RPR2 tumors, CRPR2 tumors displayed a higher number of monocytes (Fig. 3C, D). Given that myeloid-derived suppressor cells (MDSCs) inhibit T cell activation and proliferation (Nagaraj et al., 2010; Srivastava et al., 2010), we also examined the impact of CRACD loss on MDSCs. Compared to RPR2, CRPR2 tumors showed an upregulation of MDSC marker gene expression in myeloid cells (Fig. 3h, SI Appendix, Fig. S11C). Consistent with the results from the autochthonous model, immune profiling of preSC-derived allograft tumors also displayed a decrease in $CD8^+$ T cells and an increase in myeloid cells in *Cracd* KO allograft tumors relative to *Cracd* WT tumors (SI Appendix, Fig. S12, S13). These results suggest that CRACD loss induces immune landscape remodeling, which is most notable for marked $CD8^+$ T cell loss.

Epigenetic suppression of the MHC-I pathway in *Cracd* KO SCLC

The altered landscape of immune cells in *Cracd* KO SCLC tumors (Fig. 3) compelled us to determine the underlying mechanism of $CD8^+$ T cell loss. We examined the inferred intercellular communication networks between immune cells and SCLC tumor cells (RPR2 vs. CRPR2) using a CellChat package (Jin et al., 2021). Overall, this analysis suggested that CRPR2 tumors have fewer and weaker interactions among different cell types than RPR2 tumors (Fig. 4A). In the information flow maps, CRPR2 tumors displayed upregulated putative signaling pathways mainly between tumor cells and B and myeloid cells, compared to RPR2 tumors (Fig. 4B). Notably, the antigen processing and presentation–related pathways were significantly downregulated in CRPR2 tumors relative to in RPR2 tumors mostly between SCLC tumor and $CD8^+$ T cells (Fig. 4B). The information flow predicted by CellChat nominated differentially regulated pathways between RPR2 and CRPR2 tumors (Fig. 4C). According to the absolute values and fold changes of information flow, the most downregulated pathway in CRPR2 was the MHC-I pathway (Fig. 4C, SI Appendix, Fig. S14). The circle plots validated that the MHC-I pathway was barely detected in CRPR2 tumors but was prevalent in RPR2 tumors (Fig. 4D). Moreover, the GSEA confirmed the marked downregulation of the gene sets associated with the antigen processing and presentation, MHC-I pathway, and T cell receptor signaling (Fig. 4E, SI Appendix, Fig. S15). Since CRPR2 tumors displayed depleted $CD8^+$ T cells (Fig. 3), it is plausible that the impaired MHC-I pathway fails to activate $CD8^+$ T cells. We examined the expression of the MHC-I pathway–related genes. The genes (*H2-Q1/2/4* and *H2-T3*) encoding the α chain of the mouse MHC-I complex were downregulated in CRPR2 tumors

compared to RPR2 tumors (Fig. 4F). These data indicate that $CD8^+$ T cell loss in *Cracd* KO tumors is associated with MHC-I pathway suppression.

Accumulating evidence suggests that the suppression of antigen processing and presentation is one of the immune evasion mechanisms of cancer cells (Burr et al., 2019; Jhunjhunwala et al., 2021; Thompson et al., 2020). Recent studies showed that the MHC-I pathway is modulated by EZH2 (Bagai et al., 2005; Ennishi et al., 2019; Leonhardt et al., 2005; Lorenzi et al., 2012; Staehli et al., 2012). Intriguingly, GSEA of differentially expressed genes (DEGs; CRPR2 vs. RPR2) showed the association of the CRPR2 gene signatures with the genesets modulated by EZH2 and the polycomb repressive complex 2 (PRC2) that contains EZH2 as a core catalytic subunit (SI Appendix, Fig. S16A). Since EZH2 was shown to promote SCLC (Hubaux et al., 2013), these data led us to examine the role of EZH2 in suppressing the MHC-I pathway by CRACD loss. GSK343, an EZH2 inhibitor, de-repressed the expression of *H2-Q1/2/4* and *H2-T3* in the murine SCLC cell line derived from CRPR2 tumors (SI Appendix, Fig. S16B). Similarly, the human SCLC cell line (NCI-H2081) that carries a frame-shift mutation in *CRACD* (Q168Tfs*17) showed upregulation of *HLA-A/B/C* transcription by EZH2 inhibition (SI Appendix, Fig. S16C). As the catalytic subunit of PRC2, EZH2 induces di- or tri-methylation of histone H3 (H3K27me2/3), affecting transcriptional accessibility. Immunofluorescent staining and immunoblot-based quantification showed that compared to RPR2 tumors, CRPR2 tumors exhibited reduced H3K27ac, a histone mark for gene activation, and increased H3K27me2/3, histone marks for gene repression that are induced by PRC2 (SI Appendix, Fig. S16D-G). These results suggest that CRACD loss suppresses the MHC-I pathway via EZH2-mediated epigenetic repression.

Identification of SCLC patients with CRACD inactivation and MHC-I pathway suppression

To determine the relevance of the findings in *Cracd KO* SCLC in mice to human disease, we performed a cross-species comparison of SCLC transcriptomes of both species. We combined scRNA-seq datasets of 19 SCLC patient tumor samples and 8 normal human lung samples from a previous study (Chan et al., 2021; Reyfman et al., 2019) (Fig. 5A, SI Appendix, Table S7, S8) with the CRPR2 tumor scRNA-seq dataset converted into corresponding human homologs. A pair-wise correlation analysis showed that combined human tumor and CRPR2 data could be divided into two major groups (SC1- and SC2-type); CRPR2 clustered with the SC1-type tumors (Fig. 5B, SI Appendix, Fig. S17A). According to the ANPY classification (Rudin et al., 2019), the SC1-type was categorized as ASCL1-type (SI Appendix, Fig. S17A). The SC1-type SCLC tumors were clinically associated with recurrence (2 of 3) and metastasis (1 of 3), whereas the SC2-type tumors were mainly associated with primary tumors (6 of 16) and metastases (7 of 16) (Fig. 5C). A copy number variation analysis showed higher genomic instability in the SC2-type than in the SC1-type tumors (Fig. 5D, E).

Given that CRPR2 was classified as the SC1-type, we determined whether SC1-type SCLC patient tumors recapitulate the distinct features of CRPR2. The SC1-type tumors expressed relatively lower levels of *CRACD*, EZH2 target genes, PRC2 target genes, and the genes encoding MHC-I and several of the antigen processing and presentation pathway components (*HLA-A*, *B*, *C*, *E*, *LMP2/LMP7*, and *TAP1/2*) compared to the SC2-type tumors (Fig. 5F, SI Appendix, Fig. S17B-D), also confirmed by the GSEA (Fig. 5G).

We also sought biomarkers specifying the SC1-type SCLC and identified genes that were specifically expressed in the SC1- or SC2-type SCLC. The SC1-type tumors were enriched with the expression of *AGR2* (anterior gradient 2), *CEACAM6* (carcinoembryonic antigen–related cell adhesion molecule 6), *GPRC5A* (G protein-coupled receptor class C group 5 member A), and *LGALS3* (lectin, galactoside-binding, soluble 3) genes. Exclusively, the SC2-type tumors showed the upregulation of *BAZ1A*, *TMSB15A*, *HTATSF1*, and *KIF1A* (Fig. 5H). Of note, four genes (*AGR2*, *CEACAM6*, *GPCR5A*, and *LGALS3*) mainly expressed in the SC1-type are associated with poor prognosis in several solid cancers (Alavi et al., 2015; Jantscheff et al., 2003; Wang et al., 2019; Zhou et al., 2016). These results further support the pathological relevance of CRACD inactivation and MHC-I pathway suppression as potential biomarkers classifying SCLC patients.

Discussion

In this study, we found that the genetic ablation of *Cracd* accelerated SCLC tumorigenesis and increased tumor cell diversity initiated by deleting *Rb1*, *Trp53*, and *Rbl*2 alleles in the allograft and autochthonous models. It also results in marked depletion of $CD8^+$ T cells in the tumor microenvironment, which is associated with epigenetic suppression of the MHC-I pathway in tumor cells. Single-cell transcriptomic analysis of human SCLC confirmed co-occurrence of CRACD inactivation and downregulation of the MHC-I pathway. Defining the temporal specificity of a tumor suppressor along the course of tumor development is critical to understanding SCLC pathogenesis. Leveraging the salient features of the SCLC GEMM that provides a window into early- and late-stage tumor development, this study demonstrates a tumor suppressive role for CRACD in SCLC progression and immune evasion, providing novel insight into SCLC tumorigenesis and establishing a new SCLC mouse model that lacks T cell-based immune surveillance.

ICB-based immunotherapy has emerged as a promising approach for cancer therapy (Akinleye and Rasool, 2019; Bagchi et al., 2021; Robert, 2020; Topalian et al., 2016). However, it has faced the challenges including both primary and acquired therapy resistance (Kok, 2020; Morad et al., 2021; Schoenfeld and Hellmann, 2020). The determinants of durable therapeutic benefit from ICB in patients with SCLC remain poorly understood. Identification of such determinants could help individualize SCLC therapy, and inform strategies to overcome therapeutic resistance. The animal models of *Cracd* KO SCLC and transcriptomic analysis of murine and human tumors support that the loss of CRACD is associated with inactivation of MHC-I expression in tumor cells. This cell-intrinsic change is expected not only to render tumor cells evasive to $CD8^+$ cytotoxic T cells but may also secondarily result in the loss of the T cells in the tumor microenvironment, described as ‘cold tumors’ (Duan et al., 2020). Single-cell transcriptomic analysis defined an SC1-type of human SCLC characterized by inactive CRACD, EZH2-mediated gene repression, and a suppressed MHC-I pathway, distinct from the SC2-type with active CRACD and a functional MHC-I pathway. Given the MHC-I pathway suppression in the SC1-type, it is likely that SC1-type patients may not exhibit a favorable response to T cell-based ICB (i.e., non-responders). Restoring MHC-I expression in such tumors, for example, by EZH2 inhibition, may be a strategy to reverse the immune-cold phenotype typical of human SCLC. Targeting other vital epigenetic regulators, notably the lysine demethylase LSD1, has also been shown to restore the MHC-I pathway and sensitize SCLC to ICB (Hiatt et al., 2022; Nguyen et al., 2022). Whether MHC-I expression in SC1-type tumors can be restored by LSD1 inhibition remains to be determined. This study introduces a new approach to stratify SCLC patients, defining a potential predictive biomarker for the effectiveness of T cell-based ICB such as anti-PD-1 and CTLA-4 immunotherapies.

The broad transcriptional impact of CRACD inactivation is intriguing, given the known role of the capping protein in regulating actin dynamics. In transforming intestinal epithelial cells and colon cancer cells, the loss of CRACD results in β-catenin release from the cadherin-catenin-actin complex, which then activates a β-catenin-mediated oncogenic transcription program (Jung et al., 2018). However, we think it is unlikely that this CRACD/β-catenin axis explains an enhancement of SCLC tumorigenesis, since we have recently demonstrated that the β-catenin pathway is inactive and dispensable for the tumor development and continued growth of SCLC (Kim et al., 2022a). While molecular mechanisms by which loss of CRACD influences transcription remain to be determined, one mechanism could relate to its role in regulating actin cytoskeleton in the nucleus. Emerging evidence points to the newfound roles of nuclear actin (N-actin) in regulating gene expression and chromosomal architecture (Klages-Mundt et al., 2018; Kyheröinen and Vartiainen, 2020). In addition, N-actin- and actin-related proteins comprise the chromatin remodeling complex (Chang et al., 2021; Coll et al., 2020; Han et al., 2020; Mahmood et al., 2021). Thus, it is a plausible hypothesis that upon CRACD loss, deregulated N-actin alters the assembly of the chromatin remodeling complexes leading to widespread changes in gene expression, including MHC-I pathway inhibition and alteration of the composition of cell states. The molecular mechanism by which CRACD inactivation aberrantly controls the transcription of genes related to oncogenic trajectories and the MHC-I pathway remains to be determined in future studies.

Together, our integrative approaches identify CRACD as a tumor suppressor of SCLC and show that CRACD inactivation in SCLC is associated with inhibition of the antigen presentation pathway and a marked reduction in T cell infiltration. This study provides novel insight into mechanisms of SCLC development and immune evasion.

Materials and methods

Mammalian cell culture

Human embryonic kidney 293T (HEK293T) and NCI-H2081 used in this study were purchased from American Type Culture Collection (ATCC). The murine preSC cells have been previously described (Kim et al., 2016; Kim et al., 2022b). HEK293T and preSC cells were maintained in a Dulbecco's Modified Eagle's Medium (DMEM) medium containing 10% fetal bovine serum (Thermo Fisher Scientific) and 1% penicillin and streptomycin (Thermo Fisher Scientific). NCI-H2081 was maintained in DMEM: F-12 medium (5% FBS, 1% penicillin/streptomycin, 0.005 mg/mL Insulin, 0.01mg/mL Transferrin, 30 mmol/L Sodium selenite, 10 mmol/L Hydrocortisone, 10 mmol/L β-estradiol, 2 mM L-glutamine). Cells were cultured at 37°C in a humidified incubator supplied with 5% CO_2 air. Mycoplasma contamination was examined using the MycoAlert mycoplasma detection kit (Lonza). See SI Appendix, Table S1 for reagent information.

CRISPR/Cas9-based gene knockout

CRISPR/Cas9 mediated *Cracd* KO in preSC cells was performed according to Zhang laboratory's protocol (Ran et al., 2013). Control sgRNA sequence target EGFP: 5'-GGGCG AGGAG CTGTT CACCG-3'; sgRNA sequence target *Cracd*: 5'-ACACA CGGCC ATTTT GGTCA-3'. sgRNA sequence is based on our previous study (Jung et al., 2018).

Virus production and transduction

HEK293T cells in a 10-cm dish were co-transfected with 5 μg of constructs, 5 μg of plasmid Δ8.2 (Plasmid #8455, Addgene), and 3 μg of plasmid VSVG (Plasmid #8454, Addgene). Cells were incubated at 37°C, and the medium was replaced after 12 h. Virus-containing medium was collected 48 h after transfection and supplemented with 8 μg/mL polybrene to infect target cells in 6-well dishes. After 6 h, the medium was changed. After 48 h, the infected cells were selected with 2 μg/mL puromycin.

qRT-PCR

RNAs were extracted by TRIzol (Invitrogen) and used to synthesize cDNAs using the iScript cDNA synthesis kit (Biorad). qRT-PCR was performed using an Applied Biosystems 7500 Real-Time PCR machine with the primers listed in SI Appendix, Table S2. Target gene expression was normalized to that of mouse *Hprt1* and human *HPRT1*. Comparative $2^{-\Delta\Delta Ct}$ methods were used to quantify qRT-PCR results. See SI Appendix, Table S2 for primers information.

Cell proliferation and viability assays

We counted the number of cells using a hematocytometer (Bio-Rad) on growth days according to the manufacturer's protocol. Cell proliferation was determined by crystal violet staining or Cell Counting Kit-8 (Dojindo Laboratories) according to the manufacturer's protocol. For crystal violet staining, plates were rinsed with Phosphate-buffered saline (PBS), fixed with 4% paraformaldehyde solution for 20 min, and stained with crystal violet solution (0.1% crystal violet, 10% methanol) for 20 min, followed by rinsing with tap water.

Immunoblotting

Whole-cell lysates of cells were prepared using radioimmunoprecipitation assay (RIPA) buffer with protease inhibitors for 30 min at 4°C, followed by centrifugation (4°C, 13,200 r/min for 15 min). Supernatants were denatured in 5 × Sodium dodecyl-sulfate (SDS) sample buffer (200 mmol/L Tris-HCl [pH 6.8], 40% glycerol, 8% SDS, 200 mmol/L dithiothreitol, and 0.08% bromophenol blue) at 95°C for 5 min, followed by Sodium dodecyl-sulfate polyacrylamide gel electrophoresis (SDS-PAGE). We used 2% non-fat dry milk in Tris-buffered saline and Tween-20 (25 mmol/L Tris-HCl pH 8.0, 125 mmol/L NaCl, and 0.5% Tween-20) for immunoblot blocking and antibody incubation. SuperSignal West Pico and Femto reagents (Thermo Fisher Scientific) were used to detect horseradish peroxidase-conjugated secondary antibodies. Detailed information on the antibodies is shown in SI Appendix, Table S1.

Immunofluorescence microscopy

Cells were fixed for 20 min in 4% paraformaldehyde and permeabilized with 0.1% Triton X-100 (in PBS) for 10 min. After three PBS washes, cells were blocked with 2% bovine serum albumin (BSA) for 30 min at ambient temperature. Cells were then incubated with antibodies diluted in 2% BSA at 4°C overnight. After three PBS washes, the cells were incubated with 1 μg/mL Alexa Fluor 488/647-conjugated secondary antibodies (Invitrogen) by shaking at ambient temperature in the dark for 1 h. Cells were washed three times with PBS in the dark and mounted in Prolong Gold Antifade Reagent (Invitrogen). Immunofluorescent staining was observed and analyzed using confocal or fluorescent microscopes (Zeiss) and ZEN software (Zeiss).

Animals

Immunocompromised (BALB/c athymic nude) mice and C57BL/6 mice were purchased from the Jackson Laboratory (Maine, USA). Compound transgenic mice *Rb1*$^{lox/lox}$ *Trp53*$^{lox/lox}$ *Rbl2*$^{lox/lox}$ (RPR2) mice have been previously described (Kim et al., 2022b). For SCLC tumor induction, the lungs of 10-week-old mice were infected with adenoviral Cre via intratracheal instillation as previously described (DuPage et al., 2009; Kim et al., 2022b). Multiple cohorts of independent litters were analyzed to control for background effects, and both male and female mice were used. Ad-Cracd-Cre particles were produced in Vector Development Laboratory at Baylor College of Medicine. Mice were euthanized by

CO_2 asphyxiation followed by cervical dislocation at the indicated time. Tumors were harvested from euthanized mice, fixed with 10% formalin, embedded in paraffin, and sectioned at 5-μm thickness. The sections were stained with hematoxylin and eosin for histological analysis. All mice were maintained in compliance with the guidelines of the Institutional Animal Care and Use Committee of the University of Texas MD Anderson Cancer Center and the University of Virginia School of Medicine. All animal procedures were performed based on the guidelines of the Association for the Assessment and Accreditation of Laboratory Animal Care and institutional (MD Anderson and the University of Virginia) approved protocols. This study was compliant with all relevant ethical regulations regarding animal research.

Allograft assay

C57BL/6 mice (4 months old) were purchased from the Institutional Veterinary Medicine and Surgery Facility (MD Anderson Cancer Center). Each mouse (n = 6) was subcutaneously injected with 1×10^6 cells into both flanks. 3 mice were injected with *Cracd* WT cells, the other 3 mice were injected with *Cracd* KO cells. Mice were maintained in the Division of Laboratory Animal Resources facility at MD Anderson. Tumor volume was monitored and calculated by measuring with calipers every 3-4 days (volume = [length $\times$ width^2] / 2). Tumor burden was calculated by measuring all tumor lesions within the lung to account for the complete tumor burden. Twenty days after transplantation, mice were euthanized, tumors were photographed, and collected to proceed paraffin-embedding for immunostaining or for single-cell RNA sequencing (scRNA-seq).

Mouse lung tumor and allograft tumor preparation

Prior to processing, mouse SCLC and allograft tumors were decontaminated under the dissecting microscope by removing any normal and connective tissues. Then, tumors were transferred to a dry dish and minced into pieces with blades. The tissue was digested in Leibovitz's medium (Invitrogen) with 2 mg/mL Collagenase Type I (Worthington), 2 mg/mL Elastase (Worthington), and 2 mg/mL DNase I (Worthington) at 37 °C for 45 min. The tissue was triturated with a pipet every 15 min of digestion until homogenous. The digestion was stopped with FBS (Invitrogen) to a final concentration of 20%. The cells were filtered with a 70 μm cell strainer (Falcon) and spun down at 5,000 r/min for 1 min. The cell pellet was resuspended in red blood cell lysing buffer (Sigma) for 3 min, spun down at 5,000 r/min for 1 min, and washed with 1 mL ice-cold Leibovitz's medium with 10% FBS. Cells were resuspended in 1 mL ice-cold Leibovitz's medium with 10% FBS and filtered with a cell strainer (20 μm). Dead cells were removed with Dead Cell Removal Kit (Miltenyi Biotec) according to the manufacturer's instructions. Live cells were collected for 10$\times$ Genomics library preparation.

scRNA-seq library prep

Single-cell Gene Expression Library was prepared according to the guideline for the Chromium Single Cell Gene Expression 3v3.1 kit (10× Genomics). Briefly, single cells, reverse transcription (RT) reagents, Gel Beads containing barcoded oligonucleotides, and oil were loaded on a Chromium controller (10× Genomics) to generate single-cell GEMS (Gel Beads-In-Emulsions), where full-length cDNA was synthesized and barcoded for each single cell. Subsequently, the GEMS were broken and cDNAs from each single cell were pooled, followed by cleanup using Dynabeads MyOne Silane Beads and cDNA amplification by PCR. The amplified product was then fragmented to optimal size before end-repair, A-tailing, and adaptor ligation. The final library was generated by amplification. The library was performed at the Single Cell Genomics Core at BCM.

scRNA-seq - raw data processing, clustering, and annotation

The Cell Ranger was used for demultiplexing, barcoded processing, and gene counting. The R package Seurat(Hao et al., 2021) and Python package Scanpy(Wolf et al., 2018) were used for pre-processing and clustering of scRNA-seq data. UMAP was used for dimensional reduction, and cells were clustered in Seurat or Scanpy. Each cluster was annotated based on marker gene information (see SI Appendix, Table S3, S4, the list of marker genes of each cell cluster). Datasets were pre-processed, normalized separately, and annotated based on their marker gene expression. Scanpy was used for human dataset preprocessing and integration. Each dataset was normalized separately and clustered by the “Leiden” algorithm (Traag et al., 2019). Scanpy was used to concatenate the *Cracd* WT vs. KO dataset and preSC Cracd WT vs. KO samples. Cells with less than 100 genes expressed and more than 20% mitochondrial reads were removed. Genes expressed in less than 20 cells were removed. Gene expression for each cell was normalized and log-transformed. The percentages of mitochondrial reads were regressed before scaling the data. Dimensionality reduction and Leiden clustering (resolution 0.5 ~ 1) was carried out, and cell lineages were annotated based on algorithmically defined marker gene expression for each cluster (sc.tl.rank_genes_groups, method=‘wilcoxon’). The list of differentially expressed genes (DEGs) in *CRPR2 and preSC Cracd KO* was generated by comparing KO vs. WT (sc.tl.rank_genes_groups, groups=['KO'], reference='WT', method='wilcoxon'). More information about the software and algorithms used in this study is shown in SI Appendix, Table S5.

Cell lineage trajectory analysis

RNA velocity(La Manno et al., 2018) was used to predict the future state of individual cells and cell lineage tracing. Cells were filtered, and dimensional reduction was performed following the default parameters using the scVelo and Scanpy packages. RNA velocity was calculated through dynamical model and negbin model, and cells were clustered using the “Leiden” algorithm. RNA velocity for all datasets was performed with the same parameters (n_neighbors=10, n_pcs=40). Velocity streams were

analyzed and plotted by scVelo (dynamical model) (Bergen et al., 2020) and Dynamo (negbin model) (Qiu et al., 2022). Velocity pseudotime analysis was done and plotted with the scVelo package (Bergen et al., 2020) to show the cell state (differentiation vs. de-differentiation) of each cell. PAGA(Wolf et al., 2019) analysis was performed and visualized with scVelo package to predict developmental trajectories and explores the connectivity between different cell clusters.

Proportion difference analysis

Differences in clusters from the two datasets were analyzed and plotted using the pandas package (McKinney, 2010). Each cell cluster from the integrated dataset was grouped and cluster differences between the two datasets were compared.

Gene set enrichment analysis (GESA)

GSEA was done using the R package “fgsea” (Korotkevich et al., 2021) based on the DEG list generated by Scanpy. The enrichment value was calculated and plotted with the fgsea package (permutation number = 2,000).

Cell-cell communication analysis

For ligand-receptor interaction-based cell-cell communication analysis of scRNA-seq datasets the ‘CellChat’ (Jin et al., 2021) package in R (https://www.r-project.org) was used. The integrated dataset was processed using the Seurat package, then clustered and annotated dataset were analyzed by CellChat with default parameters (p-value threshold = 0.05). Epithelial cells were used as a source group, and immune cells were used as target groups.

Pathway score analysis

Scanpy with the ‘scanpy.tl.score_genes’ function was used for the pathway score analysis (Wolf et al., 2018). The analysis was performed with default parameters and the reference genes from the gene ontology biological process or the Kyoto Encyclopedia of Genes and Genomes database (Ashburner et al., 2000; Kanehisa, 1996). The gene list for the score analysis is shown in SI Appendix, Table S6.

Human scRNA-seq data analysis

The scRNA-seq data set of 19 human SCLC patients samples (Patients information is shown in SI Appendix, Table S7) (Chan et al., 2021) from Human Tumor Atlas Network (HTAN, https://humantumoratlas.org/) was downloaded and analyzed according to the code provided in the original study. The scRNA-seq data set of the 8 normal human lungs (GSE122960, SI Appendix, Table S8) (Reyfman et al., 2019) was extracted from the Gene Expression Omnibus (GEO) database and

analyzed with Scanpy and Python. First, to match the gene names of our mouse CRPR2 dataset with those of human datasets, we converted mouse gene names into human gene names using the R package biomaRt, which converted 16,780 genes into human genes. The converted CRPR2 dataset and 27 human datasets were concatenated, normalized, and clustered in Scanpy. Batch effects were corrected using "Harmony" (Korsunsky et al., 2019) algorithm. Then, the dendrogram and correlation matrix heatmap were plotted with Scanpy. The dendrogram shows the distance of each dataset based on principal component analysis, and the correlation matrix heatmap shows Pearson correlation by a color spectrum.

Copy number variation analysis

To detect the genomic stability of groups SC1 and SC2, we performed copy number variations (CNVs) analysis from the gene expression data using the Python package infercnvpy (https://icbi-lab.github.io/infercnvpy/index.html#). We ran infercnvpy on SC1 and SC2 groups using the Normal group (8 human normal lung datasets) as a reference dataset. The gene ordering file containing the chromosomal start and end position for each gene was generated from the human GRCh38 assembly. Chromosome heatmap and CNV scores in the UMAP were plotted with infercnvpy.

Public sequencing database

All TCGA cancer patients' sequencing data referenced in this study were obtained from the TCGA database at cBioPortal Cancer Genomics (http://www.cbioportal.org). Cancer cell line sequencing data from Cancer Cell Line Encyclopedia (CCLE) were extracted from the cBioPortal Cancer Genomics (http://www.cbioportal.org).

Data availability

scRNA-seq data are available via the GEO database (GSE218544; log-in token for reviewers: efsxisoijvwzhuh).

Code availability

The code used to reproduce the analyses described in this manuscript can be accessed via GitHub (https://github.com/jaeilparklab/CRACD_SCLC_scRNAseq) and will also be available upon request.

Statistical analyses

GraphPad Prism 9.4 (Dogmatics) was used for statistical analyses. The Student's *t*-test was used to compare two samples. P values < 0.05 were considered statistically significant. Error bars indicate the standard deviation (s.d.) otherwise described in Figure legends.

Acknowledgments

We are grateful to Pierre D. McCrea, Malgorzata Kloc, Rachael Miller, and Adriana Paulucci for their insightful comments and to Ann Sutton (Research Medical Library, MD Anderson) for editing the manuscript. This work was supported by the Cancer Prevention and Research Institute of Texas (RP200315 to J.-I.P.), the National Cancer Institute (R35 CA263816 to C.M.R.; U01 CA224293 to K.-S.P.; R01 CA193297 and R03 CA256207 to J.-I.P.), and an Institutional Research Grant (MD Anderson to J.-I.P.). The core facilities at MD Anderson (DNA Sequencing and Genetically Engineered Mouse Facility) were supported by National Cancer Institute Cancer Center Support Grant (P30 CA016672). The Research Histology Core at the University of Virginia was supported by National Cancer Institute Cancer Center Support Grant (P30 CA044579). The core facilities at Baylor College of Medicine (Cytometry & Cell Sorting Core and Single Cell Genomics Core) were supported by CPRIT (RP180672, RP200504) and the National Institutes of Health (CA125123, RR024574).

References

Akinleye, A., and Z. Rasool. 2019. Immune checkpoint inhibitors of PD-L1 as cancer therapeutics. *Journal of hematology & oncology* 12:1-13.

Alavi, M., V. Mah, E.L. Maresh, L. Bagryanova, S. Horvath, D. Chia, L. Goodglick, and A.Y. Liu. 2015. High expression of AGR2 in lung cancer is predictive of poor survival. *BMC cancer* 15:1-9.

Anderson, N.M., and M.C. Simon. 2020. The tumor microenvironment. *Curr Biol* 30:R921-R925.

Ashburner, M., C.A. Ball, J.A. Blake, D. Botstein, H. Butler, J.M. Cherry, A.P. Davis, K. Dolinski, S.S. Dwight, J.T. Eppig, M.A. Harris, D.P. Hill, L. Issel-Tarver, A. Kasarskis, S. Lewis, J.C. Matese, J.E. Richardson, M. Ringwald, G.M. Rubin, and G. Sherlock. 2000. Gene ontology: tool for the unification of biology. The Gene Ontology Consortium. *Nat Genet* 25:25-29.

Bagai, R., A. Valujskikh, D.H. Canaday, E. Bailey, P.N. Lalli, C.V. Harding, and P.S. Heeger. 2005. Mouse endothelial cells cross-present lymphocyte-derived antigen on class I MHC via a TAP1-and proteasome-dependent pathway. *The Journal of Immunology* 174:7711-7715.

Bagchi, S., R. Yuan, and E.G. Engleman. 2021. Immune checkpoint inhibitors for the treatment of cancer: clinical impact and mechanisms of response and resistance. *Annual Review of Pathology: Mechanisms of Disease* 16:223-249.

Bejarano, L., M.J. Jordão, and J.A. Joyce. 2021. Therapeutic targeting of the tumor microenvironment. *Cancer discovery* 11:933-959.

Bergen, V., M. Lange, S. Peidli, F.A. Wolf, and F.J. Theis. 2020. Generalizing RNA velocity to transient cell states through dynamical modeling. *Nature biotechnology* 38:1408-1414.

Bunn Jr, P.A., J.D. Minna, A. Augustyn, A.F. Gazdar, Y. Ouadah, M.A. Krasnow, A. Berns, E. Brambilla, N. Rekhtman, and P.P. Massion. 2016. Small cell lung cancer: can recent advances in biology and molecular biology be translated into improved outcomes? *Journal of Thoracic Oncology* 11:453-474.

Burr, M.L., C.E. Sparbier, K.L. Chan, Y.-C. Chan, A. Kersbergen, E.Y. Lam, E. Azidis-Yates, D. Vassiliadis, C.C. Bell, and O. Gilan. 2019. An evolutionarily conserved function of polycomb silences the MHC class I antigen presentation pathway and enables immune evasion in cancer. *Cancer cell* 36:385-401. e388.

Byers, L.A., and C.M. Rudin. 2015. Small cell lung cancer: where do we go from here? *Cancer* 121:664-672.

Chan, J.M., Á. Quintanal-Villalonga, V.R. Gao, Y. Xie, V. Allaj, O. Chaudhary, I. Masilionis, J. Egger, A. Chow, and T. Walle. 2021. Signatures of plasticity, metastasis, and immunosuppression in an atlas of human small cell lung cancer. *Cancer Cell* 39:1479-1496. e1418.

Chang, C.-Y., Z. Shipony, S.G. Lin, A. Kuo, X. Xiong, K.M. Loh, W.J. Greenleaf, and G.R. Crabtree. 2021. Increased ACTL6A occupancy within mSWI/SNF chromatin remodelers drives human squamous cell carcinoma. *Molecular Cell* 81:4964-4978. e4968.

546 Coll, A.P., M. Chen, P. Taskar, D. Rimmington, S. Patel, J.A. Tadross, I. Cimino, M. Yang, P.
547 Welsh, and S. Virtue. 2020. Structure of SWI/SNF chromatin remodeller RSC bound to a
548 nucleosome.
549 Duan, Q., H. Zhang, J. Zheng, and L. Zhang. 2020. Turning cold into hot: firing up the tumor
550 microenvironment. *Trends in cancer* 6:605-618.
551 DuPage, M., A.L. Dooley, and T. Jacks. 2009. Conditional mouse lung cancer models using
552 adenoviral or lentiviral delivery of Cre recombinase. *Nature protocols* 4:1064-1072.
553 Ennishi, D., K. Takata, W. Béguelin, G. Duns, A. Mottok, P. Farinha, A. Bashashati, S. Saberi, M.
554 Boyle, and B. Meissner. 2019. Molecular and Genetic Characterization of MHC
555 Deficiency Identifies EZH2 as Therapeutic Target for Enhancing Immune
556 RecognitionMolecular Profile of MHC Deficiency. *Cancer discovery* 9:546-563.
557 Gay, C.M., C.A. Stewart, E.M. Park, L. Diao, S.M. Groves, S. Heeke, B.Y. Nabet, J. Fujimoto,
558 L.M. Solis, and W. Lu. 2021. Patterns of transcription factor programs and immune
559 pathway activation define four major subtypes of SCLC with distinct therapeutic
560 vulnerabilities. *Cancer cell* 39:346-360. e347.
561 Gazdar, A.F., P.A. Bunn, and J.D. Minna. 2017. Small-cell lung cancer: what we know, what we
562 need to know and the path forward. *Nature Reviews Cancer* 17:725-737.
563 Gazdar, A.F., T.K. Savage, J.E. Johnson, A. Berns, J. Sage, R.I. Linnoila, D. MacPherson, D.G.
564 McFadden, A. Farago, and T. Jacks. 2015. The comparative pathology of genetically
565 engineered mouse models for neuroendocrine carcinomas of the lung. *Journal of*
566 *thoracic oncology* 10:553-564.
567 George, J., J.S. Lim, S.J. Jang, Y. Cun, L. Ozretić, G. Kong, F. Leenders, X. Lu, L. Fernández-
568 Cuesta, and G. Bosco. 2015. Comprehensive genomic profiles of small cell lung cancer.
569 *Nature* 524:47-53.
570 Gulati, G.S., S.S. Sikandar, D.J. Wesche, A. Manjunath, A. Bharadwaj, M.J. Berger, F. Ilagan,
571 A.H. Kuo, R.W. Hsieh, and S. Cai. 2020. Single-cell transcriptional diversity is a hallmark
572 of developmental potential. *Science* 367:405-411.
573 Han, Y., A.A. Reyes, S. Malik, and Y. He. 2020. Cryo-EM structure of SWI/SNF complex bound
574 to a nucleosome. *Nature* 579:452-455.
575 Hao, Y., S. Hao, E. Andersen-Nissen, W.M. Mauck III, S. Zheng, A. Butler, M.J. Lee, A.J. Wilk, C.
576 Darby, and M. Zager. 2021. Integrated analysis of multimodal single-cell data. *Cell*
577 184:3573-3587. e3529.
578 Hiatt, J.B., H. Sandborg, S.M. Garrison, H.U. Arnold, S.-Y. Liao, J.P. Norton, T.J. Friesen, F. Wu,
579 K.D. Sutherland, and H.Y. Rienhoff Jr. 2022. Inhibition of LSD1 with Bomedemstat
580 Sensitizes Small Cell Lung Cancer to Immune Checkpoint Blockade and T-Cell Killing.
581 *Clinical Cancer Research* 28:4551-4564.
582 Howlader, N., A. Noone, M.e. Krapcho, D. Miller, A. Brest, M. Yu, J. Ruhl, Z. Tatalovich, A.
583 Mariotto, and D. Lewis. 2019. SEER cancer statistics review, 1975–2016. *National Cancer*
584 *Institute* 1:
585 Hubaux, R., K.L. Thu, B.P. Coe, C. MacAulay, S. Lam, and W.L. Lam. 2013. EZH2 promotes
586 E2F-driven SCLC tumorigenesis through modulation of apoptosis and cell-cycle
587 regulation. *Journal of Thoracic Oncology* 8:1102-1106.
588 Iams, W.T., J. Porter, and L. Horn. 2020. Immunotherapeutic approaches for small-cell lung
589 cancer. *Nature Reviews Clinical Oncology* 17:300-312.

590 Ireland, A.S., A.M. Micinski, D.W. Kastner, B. Guo, S.J. Wait, K.B. Spainhower, C.C. Conley,
591 O.S. Chen, M.R. Guthrie, and D. Soltero. 2020. MYC drives temporal evolution of small
592 cell lung cancer subtypes by reprogramming neuroendocrine fate. *Cancer cell* 38:60-78.
593 e12.
594 Jantscheff, P., L. Terracciano, A. Lowy, K. Glatz-Krieger, F. Grunert, B. Micheel, J. Brümmer, U.
595 Laffer, U. Metzger, and R. Herrmann. 2003. Expression of CEACAM6 in resectable
596 colorectal cancer: a factor of independent prognostic significance. *Journal of clinical*
597 *oncology* 21:3638-3646.
598 Jhunjhunwala, S., C. Hammer, and L. Delamarre. 2021. Antigen presentation in cancer: insights
599 into tumour immunogenicity and immune evasion. *Nature Reviews Cancer* 21:298-312.
600 Jia, D., A. Augert, D.-W. Kim, E. Eastwood, N. Wu, A.H. Ibrahim, K.-B. Kim, C.T. Dunn, S.P.
601 Pillai, and A.F. Gazdar. 2018. Crebbp loss drives small cell lung cancer and increases
602 sensitivity to HDAC inhibition. *Cancer discovery* 8:1422-1437.
603 Jin, S., C.F. Guerrero-Juarez, L. Zhang, I. Chang, R. Ramos, C.-H. Kuan, P. Myung, M.V. Plikus,
604 and Q. Nie. 2021. Inference and analysis of cell-cell communication using CellChat.
605 *Nature communications* 12:1-20.
606 Jung, Y.S., W. Wang, S. Jun, J. Zhang, M. Srivastava, M.J. Kim, E.M. Lien, J. Shang, J. Chen,
607 P.D. McCrea, S. Zhang, and J.I. Park. 2018. Deregulation of CRAD-controlled
608 cytoskeleton initiates mucinous colorectal cancer via beta-catenin. *Nat Cell Biol*
609 20:1303-1314.
610 Kanehisa, M. 1996. Toward pathway engineering: a new database of genetic and molecular
611 pathways. *Sci. Technol. Jap.* 59:34-38.
612 Kim, D.-W., K.-C. Kim, K.-B. Kim, C.T. Dunn, and K.-S. Park. 2018. Transcriptional deregulation
613 underlying the pathogenesis of small cell lung cancer. *Translational lung cancer research*
614 7:4.
615 Kim, D.-W., N. Wu, Y.-C. Kim, P.F. Cheng, R. Basom, D. Kim, C.T. Dunn, A.Y. Lee, K. Kim, and
616 C.S. Lee. 2016. Genetic requirement for Mycl and efficacy of RNA Pol I inhibition in
617 mouse models of small cell lung cancer. *Gene Dev* 30:1289-1299.
618 Kim, K.-B., D.-W. Kim, Y. Kim, J. Tang, N. Kirk, Y. Gan, B. Kim, B. Fang, J.-I. Park, and Y.
619 Zheng. 2022a. WNT5A–RHOA Signaling Is a Driver of Tumorigenesis and Represents a
620 Therapeutically Actionable Vulnerability in Small Cell Lung Cancer. *Cancer Research*
621 82:4219-4233.
622 Kim, K.B., A. Kabra, D.W. Kim, Y. Xue, Y. Huang, P.C. Hou, Y. Zhou, L.J. Miranda, J.I. Park, X.
623 Shi, T.P. Bender, J.H. Bushweller, and K.S. Park. 2022b. KIX domain determines a
624 selective tumor-promoting role for EP300 and its vulnerability in small cell lung cancer.
625 *Sci Adv* 8:eabl4618.
626 Klages-Mundt, N.L., A. Kumar, Y. Zhang, P. Kapoor, and X. Shen. 2018. The nature of actin-
627 family proteins in chromatin-modifying complexes. *Frontiers in genetics* 9:398.
628 Kok, V.C. 2020. Current understanding of the mechanisms underlying immune evasion from
629 PD-1/PD-L1 immune checkpoint blockade in head and neck cancer. *Frontiers in oncology*
630 10:268.
631 Korotkevich, G., V. Sukhov, N. Budin, B. Shpak, M.N. Artyomov, and A. Sergushichev. 2021.
632 Fast gene set enrichment analysis. *BioRxiv* 060012.

633 Korsunsky, I., N. Millard, J. Fan, K. Slowikowski, F. Zhang, K. Wei, Y. Baglaenko, M. Brenner,
634 P.-r. Loh, and S. Raychaudhuri. 2019. Fast, sensitive and accurate integration of single-
635 cell data with Harmony. *Nature methods* 16:1289-1296.
636 Kyheröinen, S., and M.K. Vartiainen. 2020. Nuclear actin dynamics in gene expression and
637 genome organization. In Seminars in cell & developmental biology. Elsevier, 105-112.
638 La Manno, G., R. Soldatov, A. Zeisel, E. Braun, H. Hochgerner, V. Petukhov, K. Lidschreiber,
639 M.E. Kastriti, P. Lönnerberg, A. Furlan, J. Fan, L.E. Borm, Z. Liu, D. van Bruggen, J. Guo,
640 X. He, R. Barker, E. Sundström, G. Castelo-Branco, P. Cramer, I. Adameyko, S.
641 Linnarsson, and P.V. Kharchenko. 2018. RNA velocity of single cells. *Nature* 560:494-
642 498.
643 Leonhardt, R.M., K. Keusekotten, C. Bekpen, and M.R. Knittler. 2005. Critical role for the
644 tapasin-docking site of TAP2 in the functional integrity of the MHC class I-peptide-
645 loading complex. *The Journal of Immunology* 175:5104-5114.
646 Lorenzi, S., M. Forloni, L. Cifaldi, C. Antonucci, A. Citti, R. Boldrini, M. Pezzullo, A. Castellano,
647 V. Russo, and P. van der Bruggen. 2012. IRF1 and NF-kB restore MHC class I-restricted
648 tumor antigen processing and presentation to cytotoxic T cells in aggressive
649 neuroblastoma.
650 Mahmood, S.R., X. Xie, N. Hosny El Said, T. Venit, K.C. Gunsalus, and P. Percipalle. 2021. β-
651 actin dependent chromatin remodeling mediates compartment level changes in 3D
652 genome architecture. *Nature communications* 12:1-15.
653 McKinney, W. 2010. Data structures for statistical computing in python. In Proceedings of the
654 9th Python in Science Conference. Austin, TX, 51-56.
655 Morad, G., B.A. Helmink, P. Sharma, and J.A. Wargo. 2021. Hallmarks of response, resistance,
656 and toxicity to immune checkpoint blockade. *Cell* 184:5309-5337.
657 Nagaraj, S., A.G. Schrum, H.-I. Cho, E. Celis, and D.I. Gabrilovich. 2010. Mechanism of T cell
658 tolerance induced by myeloid-derived suppressor cells. *The Journal of Immunology*
659 184:3106-3116.
660 Ng, S.R., W.M. Rideout III, E.H. Akama-Garren, A. Bhutkar, K.L. Mercer, J.M. Schenkel, R.T.
661 Bronson, and T. Jacks. 2020. CRISPR-mediated modeling and functional validation of
662 candidate tumor suppressor genes in small cell lung cancer. *Proceedings of the National*
663 *Academy of Sciences* 117:513-521.
664 Nguyen, E.M., H. Taniguchi, J.M. Chan, Y.A. Zhan, X. Chen, J. Qiu, E. de Stanchina, V. Allaj,
665 N.S. Shah, and F. Uddin. 2022. Targeting Lysine-Specific Demethylase 1 Rescues Major
666 Histocompatibility Complex Class I Antigen Presentation and Overcomes Programmed
667 Death-Ligand 1 Blockade Resistance in SCLC. *Journal of thoracic oncology: official*
668 *publication of the International Association for the Study of Lung Cancer* 17:1014-1031.
669 Pakkala, S., and T.K. Owonikoko. 2018. Immune checkpoint inhibitors in small cell lung cancer.
670 *Journal of thoracic disease* 10:S460.
671 Peifer, M., L. Fernández-Cuesta, M.L. Sos, J. George, D. Seidel, L.H. Kasper, D. Plenker, F.
672 Leenders, R. Sun, and T. Zander. 2012. Integrative genome analyses identify key
673 somatic driver mutations of small-cell lung cancer. *Nature genetics* 44:1104-1110.
674 Qiu, X., Y. Zhang, J.D. Martin-Rufino, C. Weng, S. Hosseinzadeh, D. Yang, A.N. Pogson, M.Y.
675 Hein, K. Hoi Min, L. Wang, E.I. Grody, M.J. Shurtleff, R. Yuan, S. Xu, Y. Ma, J.M.

676 Replogle, E.S. Lander, S. Darmanis, I. Bahar, V.G. Sankaran, J. Xing, and J.S. Weissman.
677 2022. Mapping transcriptomic vector fields of single cells. *Cell* 185:690-711.e645.
678 Ragavan, M., and M. Das. 2020. Systemic Therapy of Extensive Stage Small Cell Lung Cancer
679 in the Era of Immunotherapy. *Curr Treat Options Oncol* 21:64.
680 Ran, F., P.D. Hsu, J. Wright, V. Agarwala, D.A. Scott, and F. Zhang. 2013. Genome engineering
681 using the CRISPR-Cas9 system. *Nature protocols* 8:2281-2308.
682 Reyfman, P.A., J.M. Walter, N. Joshi, K.R. Anekalla, A.C. McQuattie-Pimentel, S. Chiu, R.
683 Fernandez, M. Akbarpour, C.-I. Chen, and Z. Ren. 2019. Single-cell transcriptomic
684 analysis of human lung provides insights into the pathobiology of pulmonary fibrosis.
685 *American journal of respiratory and critical care medicine* 199:1517-1536.
686 Robert, C. 2020. A decade of immune-checkpoint inhibitors in cancer therapy. *Nature*
687 *Communications* 11:1-3.
688 Rudin, C.M., J.T. Poirier, L.A. Byers, C. Dive, A. Dowlati, J. George, J.V. Heymach, J.E. Johnson,
689 J.M. Lehman, D. MacPherson, P.P. Massion, J.D. Minna, T.G. Oliver, V. Quaranta, J.
690 Sage, R.K. Thomas, C.R. Vakoc, and A.F. Gazdar. 2019. Molecular subtypes of small cell
691 lung cancer: a synthesis of human and mouse model data. *Nature Reviews Cancer*
692 19:289-297.
693 Schaffer, B.E., K.-S. Park, G. Yiu, J.F. Conklin, C. Lin, D.L. Burkhart, A.N. Karnezis, E.A. Sweet-
694 Cordero, and J. Sage. 2010. Loss of p130 Accelerates Tumor Development in a Mouse
695 Model for Human Small-Cell Lung CarcinomaRb, p53, and p130 Collaboratively
696 Suppress SCLC. *Cancer research* 70:3877-3883.
697 Schoenfeld, A.J., and M.D. Hellmann. 2020. Acquired resistance to immune checkpoint
698 inhibitors. *Cancer cell* 37:443-455.
699 Srivastava, M.K., P. Sinha, V.K. Clements, P. Rodriguez, and S. Ostrand-Rosenberg. 2010.
700 Myeloid-derived suppressor cells inhibit T-cell activation by depleting cystine and
701 cysteine. *Cancer research* 70:68-77.
702 Staehli, F., K. Ludigs, L.X. Heinz, Q. Seguín-Estévez, I. Ferrero, M. Braun, K. Schroder, M.
703 Rebsamen, A. Tardivel, and C. Mattmann. 2012. NLRC5 deficiency selectively impairs
704 MHC class I-dependent lymphocyte killing by cytotoxic T cells. *The Journal of*
705 *Immunology* 188:3820-3828.
706 Thompson, J.C., C. Davis, C. Deshpande, W.-T. Hwang, S. Jeffries, A. Huang, T.C. Mitchell, C.J.
707 Langer, and S.M. Albelda. 2020. Gene signature of antigen processing and presentation
708 machinery predicts response to checkpoint blockade in non-small cell lung cancer
709 (NSCLC) and melanoma. *Journal for immunotherapy of cancer* 8:
710 Topalian, S.L., J.M. Taube, R.A. Anders, and D.M. Pardoll. 2016. Mechanism-driven biomarkers
711 to guide immune checkpoint blockade in cancer therapy. *Nature Reviews Cancer* 16:275-
712 287.
713 Traag, V.A., L. Waltman, and N.J. Van Eck. 2019. From Louvain to Leiden: guaranteeing well-
714 connected communities. *Sci Rep-Uk* 9:1-12.
715 Wang, H., X. Song, Q. Huang, T. Xu, D. Yun, Y. Wang, L. Hu, Y. Yan, H. Chen, and D. Lu. 2019.
716 LGALS3 promotes treatment resistance in glioblastoma and is associated with tumor
717 risk and prognosis. *Cancer Epidemiology, Biomarkers & Prevention* 28:760-769.
718 Wolf, F.A., P. Angerer, and F.J. Theis. 2018. SCANPY: large-scale single-cell gene expression
719 data analysis. *Genome Biology* 19:15.

720 Wolf, F.A., F.K. Hamey, M. Plass, J. Solana, J.S. Dahlin, B. Göttgens, N. Rajewsky, L. Simon,
721 and F.J. Theis. 2019. PAGA: graph abstraction reconciles clustering with trajectory
722 inference through a topology preserving map of single cells. *Genome Biology* 20:59.
723 Zhou, H., A. Telonis, Y. Jing, N. Xia, L. Biederman, M. Jimbo, F. Blanco, E. Londin, J. Brody, and
724 I. Rigoutsos. 2016. GPRC5A is a potential oncogene in pancreatic ductal
725 adenocarcinoma cells that is upregulated by gemcitabine with help from HuR. *Cell*
726 *death & disease* 7:e2294-e2294.
727
728
729

Figures legends

Figure 1. *Cracd* KO accelerates SCLC development in vitro and in vivo

A-C, Mouse preSCs were engineered to target *Cracd* alleles using CRISPR-mediated gene editing and characterized for cell morphology (A), short-term proliferation (B), and colony-forming ability (C). Of note, *Cracd*-targeted preSCs readily formed aggregates and spheres typical of SCLC cells. **D,** Representative images of allograft tumors (arrows) derived from preSCs (*Cracd* WT vs. KO) in the flanks of athymic nude mice. **E,** Quantification of tumor development (tumor weight / days taken to reach end-point) in the allograft model. **F-I,** Analysis of autochthonous mouse models: RPR2 (*Rb1, Trp53, Rbl2* triple KO) vs. CRPR2 (*Cracd, Rb1, Trp53, Rbl2* quadruple KO). Representative images of whole lungs (RPR2 vs. CRPR2) (F) and hematoxylin-and-eosin–stained lung sections (G). Tumor burden (H) and proliferative cell quantification (I). **J,** MKI67 immunostaining of RPR2 and CRPR2 tumors. Nuclei were counterstained with DAPI. Scale bars = 40 μm. **K,** Quantification of MKI67 fluorescence signal per 660 μm^2 in RPR2 and CRPR2 tumors. Representative images are shown. *P* values were calculated using the Student's *t*-test; error bars: standard deviation (SD).

Figure 2. Increased intratumoral heterogeneity in *Cracd* KO SCLC tumors

A, UMAPs of the scRNA-seq datasets of RPR2 and CRPR2 SCLC tumors. **B,** UMAPs of subsets of cells from the global level (left) to SCLC tumor epithelial cells (right). Each dot represents a single cell, colored by cell type. Tumor epithelial cells (RPR2 and CRPR2) were replotted into another UMAP (right). **C,** UMAPs of cell types within RPR2 (left) and CRPR2 cell subsets (right). The top two genes that were highly expressed in each cluster were used for cell cluster annotation of the UMAPs. **D,** Comparison of proportions of different cell types between the RPR2 and CRPR2 datasets. **E,** CytoTRACE scores of RPR2 and CRPR2 datasets were analyzed and plotted. **F,** Boxplots of the cell differentiation potential of each cell cluster based on the CytoTRACE score analysis; diff.: cell differentiation; **: $P < 0.01$; ***: $P < 0.001$. **G,** GSEA of gene sets associated with the epithelial-mesenchymal transition pathway and hypoxia pathway in cluster 4 in CRPR2 datasets compared to in RPR2 scRNA-seq datasets; NES, normalized enrichment score. **H,** Feature plots displaying the expression of epithelial-mesenchymal transition marker *Vim* and *Fn1*, hypoxia marker *Hif1a*. **I,** Violin (left) and feature (right) plots visualizing *Ascl1* and *Calca* expression between RPR2 and CRPR2 datasets.

Figure 3. Immune landscape remodeling in *Cracd* KO SCLC tumors

A, UMAPs of cells from the global level (left; modified from Figure 3B) and immune cell subsets (right) in RPR2 and CRPR2 scRNA-seq datasets. Each dot represents a single cell, colored by cell type. **B,** UMAP

of re-clustered whole immune cells of integrated RPR2 and CRPR2 datasets (left). Each cluster represents different immune cell types. Feature plots displaying the expression of T cell marker *Cd3d* and *Cd3g*; B cell marker *Cd79a;* NK cell marker Nkg7; Myeloid cell marker *Lyz2* and *Cd68* (right). **C,** UMAPs of RPR2 (left) and CRPR2 subsets (right) show different immune cell types. **D,** Comparison of cell proportions of each immune cell type between RPR2 and CRPR2 datasets, color-coded by clusters and cell types. **E,** Feature plots of *Cd8a* and *Mki67* expression in immune cells between RPR2 and CRPR2 datasets. **F, G,** Analysis of tumor-infiltrated $CD8^+$ T cells. Immunostaining of RPR2 and CRPR2 tumors with anti-CD8 antibody (F). Nuclei were counterstained with DAPI. Quantification of $CD8^+$ T cell counts per 660 μm^2 in RPR2 and CRPR2 tumor tissue (G). Representative images are shown. *P* values were calculated using the Student's *t*-test; error bars: SD. **H**, Dot plot showing the expression level of MDSC marker genes (*Itgam*, *Cd14*, *Clec4d/e*, *Il1b*, *Arg2*, *Wfdc17*, and *Cd300ld*) in RPR2 and CRPR2 datasets.

Figure 4. MHC-I pathway downregulation by *Cracd* KO

A, Total cell-cell interactions (left) and interaction strength (right) from RPR2 and CRPR2 tumors were analyzed using the CellChat package. **B,** Chord plots showing up-regulated (left) and down-regulated (right) signaling pathways in the CRPR2 scRNA-seq dataset compared to the RPR2 dataset, analyzed using CellChat. The inner bar colors represent the cell clusters that receive signals. The inner bar size is proportional to the signal strength received by the cell clusters. Chords indicate ligand-receptor pairs that mediate the interaction between two cell clusters. The chord size is proportional to the signal strength of the given ligand-receptor pair. Of note, for a CellChat analysis, RPR2 and CRPR2 scRNA-seq datasets were reanalyzed and reannotated with the R package Seurat. Tumor cells were subclustered into nine clusters for CellChat. **C,** Overall information flow (upper) and relative information flow (lower) of each signaling pathway in RPR2 and CRPR2 tumors, analyzed using CellChat. **D,** Circle plots displaying the inferred network of the MHC-I signaling pathway in RPR2 (left) and CRPR2 tumors (right); the thickness of each line connecting the cell clusters indicates the interaction strength, analyzed using CellChat. **E,** GSEA of gene sets associated with the MHC-I pathway in CRPR2 datasets compared to in RPR2 scRNA-seq datasets; NES, normalized enrichment score. **F,** Dot plot displaying the expression level of the MHC-I pathway–related genes in the RPR2 and CRPR2 datasets.

Figure 5. Pathological relevance of CRPR2 to human SCLC

A, UMAPs of SCLC tumor cells from 19 SCLC patient tumor samples (54,633 cells) and 8 normal lung samples (24,041 cells). Each dot represents a single cell, colored by a human sample ID (left) or SCLC vs. normal (right). **B,** Correlation matrix plot showing pair-wise correlations among the human normal lung samples, 19 patient tumor samples, and CRPR2. The dendrogram shows the distance of each dataset on the basis of principal component analysis, and the Pearson correlation is displayed with a color spectrum.

Groups of patients were categorized by dendrogram and correlation. **C,** Sankey plot shows the correlation between group SC1- and SC2-type and RU1108a and clinical information (cancer type and stage). **D, E,** A copy number variation analysis of SC1- and SC2-type tumors. Copy number variation plot showing the distribution of genomic alterations (gains and loss) in SC1- and SC2-type tumors compared with healthy human lung samples (d). Copy number variation scores were projected into the UMAP of the scRNA-seq dataset from healthy human lung samples and SC1- and SC2-type samples (e). **F,** Dot plot showing the expression of the *CRACD* gene, EZH2 target genes, PRC2 target genes, and MHC-I pathway genes in human SCLC tumor samples (SC1- and SC2-type). **G,** GSEA of gene sets associated with EZH2 targets, PRC2 targets, the MHC-I pathway, and antigen-processing and presentation in SC1- compared to SC2-type tumors. **H,** Representative marker gene expression of SC1- and SC2-type tumors were visualized for each patient. Genes that were specifically expressed in each group were selected from the differentially expressed gene analysis using the Wilcoxon method.

Figure 1

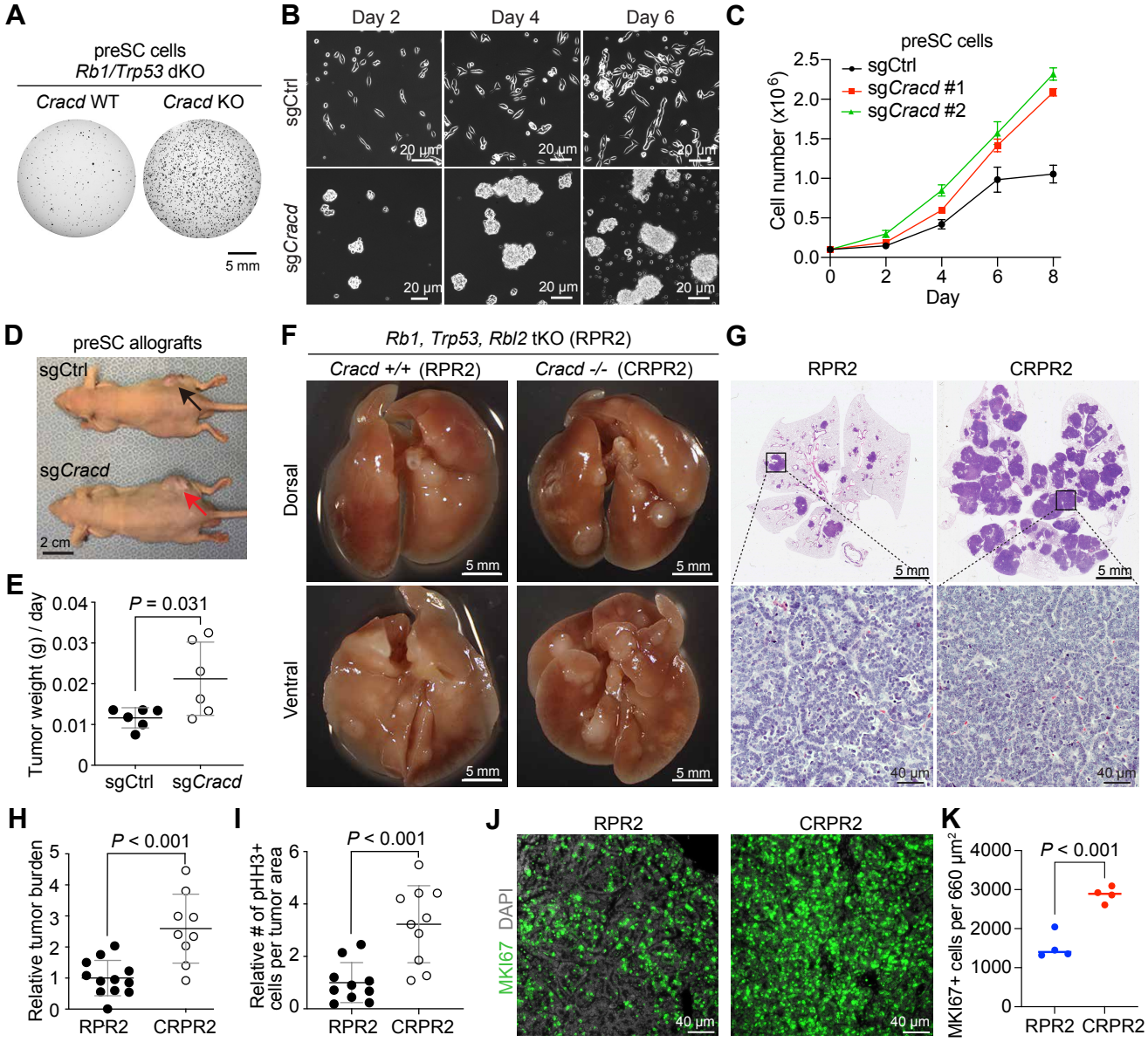
A
preSC cells
Rb1/Trp53 dKO
Cracd WT
Cracd KO
5 mm
B
Day 2
Day 4
Day 6
sgCtrl
sgCracd
20 µm
C
preSC cells
sgCtrl
sgCracd #1
sgCracd #2
Cell number (x10^6)
Day
D
preSC allografts
sgCtrl
sgCracd
2 cm
E
P = 0.031
Tumor weight (g) / day
sgCtrl
sgCracd
F
Rb1, Trp53, Rbl2 tKO (RPR2)
Cracd +/+ (RPR2)
Cracd -/- (CRPR2)
Dorsal
Ventral
5 mm
G
RPR2
CRPR2
40 µm
H
P < 0.001
Relative tumor burden
RPR2
CRPR2
I
P < 0.001
Relative # of pHH3+ cells per tumor area
RPR2
CRPR2
J
RPR2
CRPR2
MKI67
DAPI
40 µm
K
P < 0.001
MKI67+ cells per 660 µm²
RPR2
CRPR2

Figure 2

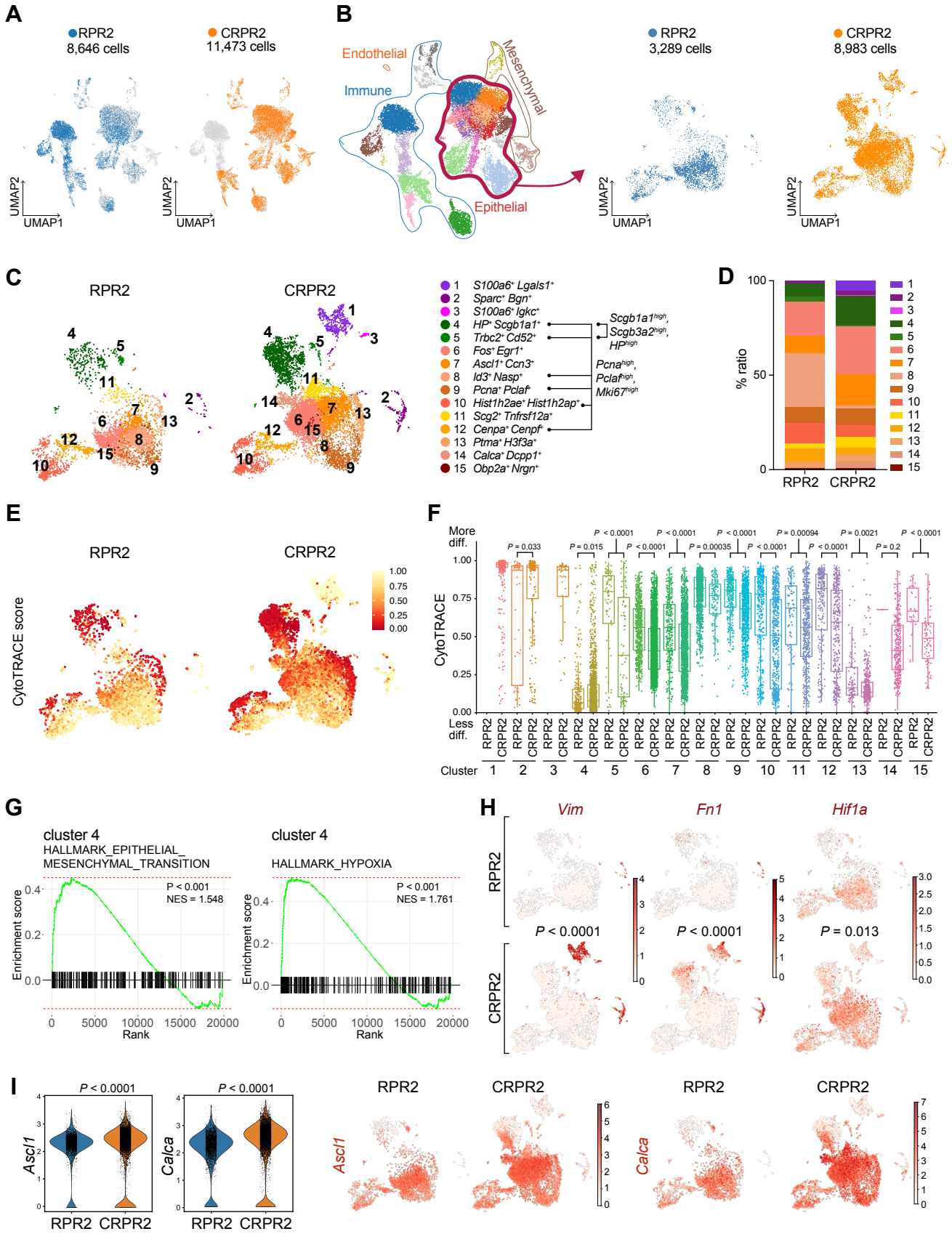
A
RPR2
8,646 cells
CRPR2
11,473 cells
UMAP2
UMAP1
B
Endothelial
Immune
Mesenchymal
Epithelial
RPR2
3,289 cells
CRPR2
8,983 cells
C
RPR2
CRPR2
1 S100a6+ Lgals1+
2 Sparc+ Bgn+
3 S100a6+ Igkc+
4 HP+ Scgb1a1+
5 Trbc2+ Cd52+
6 Fos+ Egr1+
7 Ascl1+ Ccn3+
8 Id3+ Nasp+
9 Pcna+ Pclaf+
10 Hist1h2ae+ Hist1h2ap+
11 Scg2+ Tnfrsf12a+
12 Cenpa+ Cenpf+
13 Ptma+ H3f3a+
14 Calca+ Dcpp1+
15 Obp2a+ Nrgn+
Scgb1a1high, Scgb3a2high, HPhigh
Pcnahigh, Pclafhigh, Mki67high
D
% ratio
RPR2
CRPR2
E
RPR2
CRPR2
CytoTRACE score
F
More diff.
Less diff.
CytoTRACE
Cluster
G
cluster 4
HALLMARK_EPITHELIAL_MESENCHYMAL_TRANSITION
P < 0.001
NES = 1.548
cluster 4
HALLMARK_HYPOXIA
P < 0.001
NES = 1.761
Enrichment score
Rank
H
Vim
Fn1
Hif1a
RPR2
CRPR2
P < 0.0001
P < 0.0001
P = 0.013
I
P < 0.0001
P < 0.0001
Ascl1
Calca
RPR2
CRPR2

Figure 3

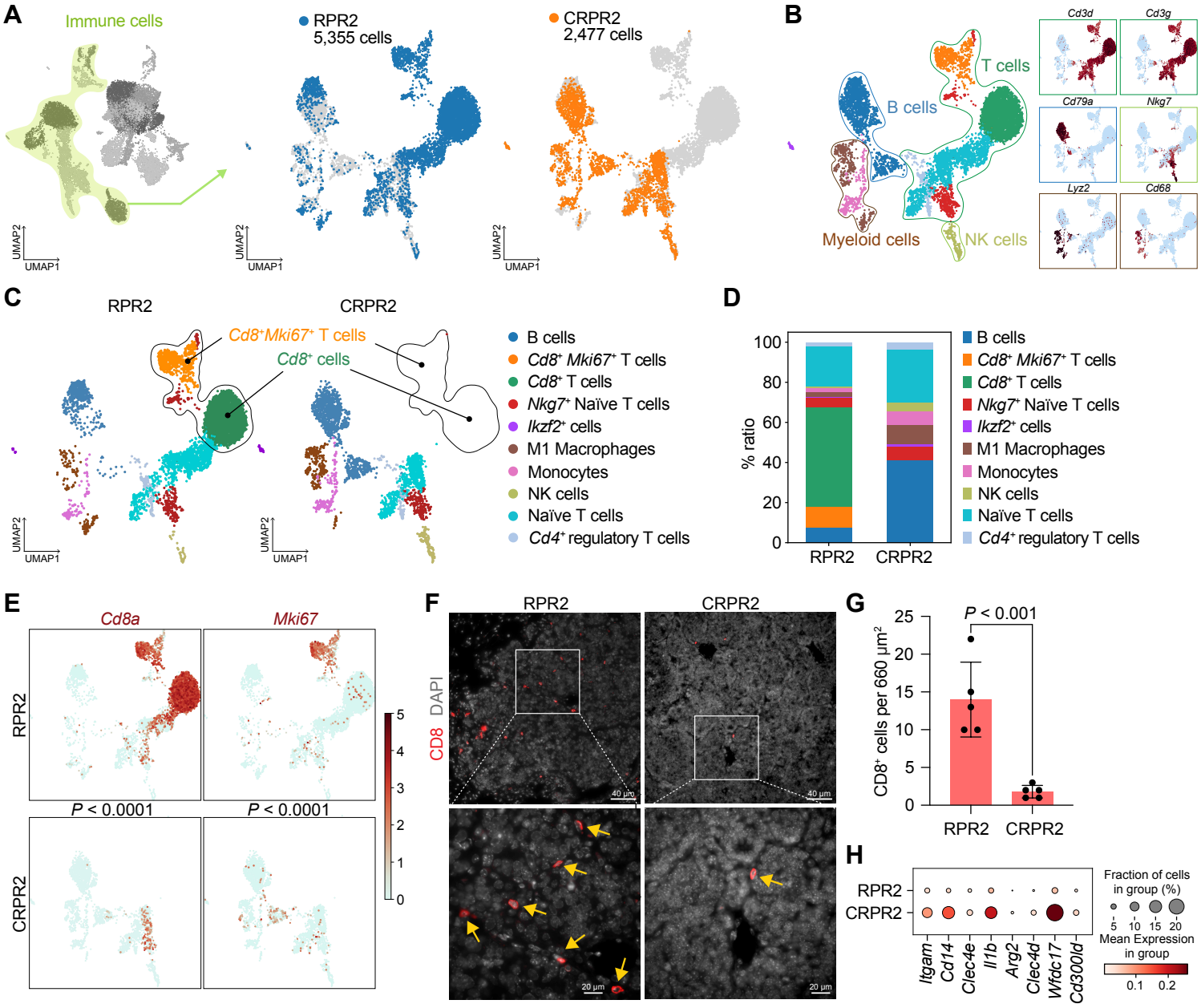
A
Immune cells
RPR2
5,355 cells
CRPR2
2,477 cells
UMAP2
UMAP1
B
T cells
B cells
Myeloid cells
NK cells
Cd3d
Cd3g
Cd79a
Nkg7
Lyz2
Cd68
C
RPR2
CRPR2
Cd8+Mki67+ T cells
Cd8+ cells
B cells
Cd8+ Mki67+ T cells
Cd8+ T cells
Nkg7+ Naïve T cells
Ikzf2+ cells
M1 Macrophages
Monocytes
NK cells
Naïve T cells
Cd4+ regulatory T cells
D
% ratio
100
80
60
40
20
0
RPR2
CRPR2
E
Cd8a
Mki67
RPR2
CRPR2
P < 0.0001
P < 0.0001
5
4
3
2
1
0
F
RPR2
CRPR2
CD8 DAPI
40 µm
20 µm
G
P < 0.001
CD8+ cells per 660 µm2
25
20
15
10
5
0
RPR2
CRPR2
H
RPR2
CRPR2
Itgam
Cd14
Clec4e
Il1b
Arg2
Clec4d
Wfdc17
Cd300ld
Fraction of cells in group (%)
5
10
15
20
Mean Expression in group
0.1
0.2

Figure 4

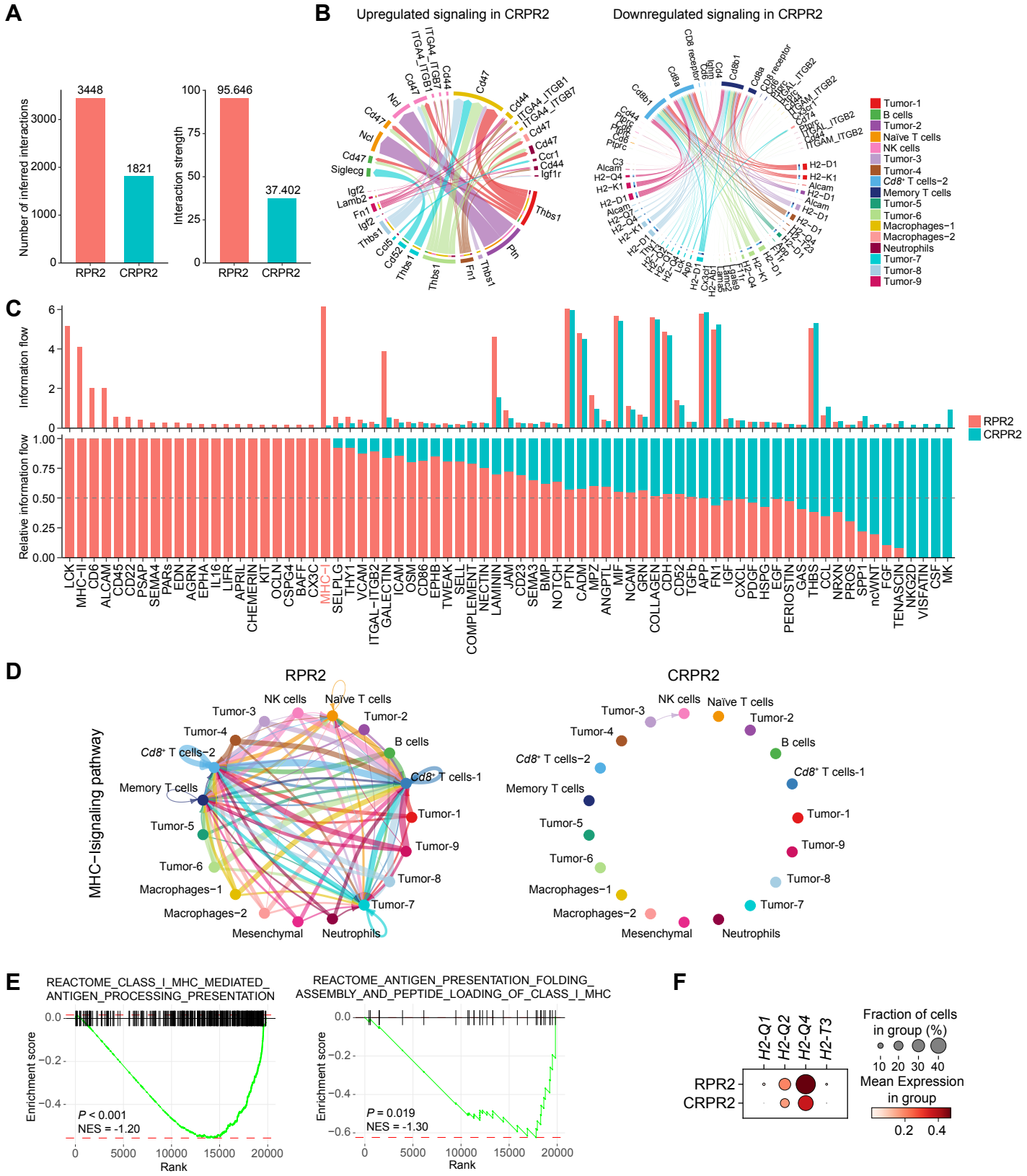
A
Number of inferred interactions
3448
1821
RPR2
CRPR2
Interaction strength
95.646
37.402
B
Upregulated signaling in CRPR2
Downregulated signaling in CRPR2
Tumor-1
B cells
Tumor-2
Naïve T cells
NK cells
Tumor-3
Tumor-4
Cd8+ T cells−2
Memory T cells
Tumor-5
Tumor-6
Macrophages−1
Macrophages−2
Neutrophils
Tumor-7
Tumor-8
Tumor-9
C
Information flow
Relative information flow
RPR2
CRPR2
D
RPR2
CRPR2
MHC−Isignaling pathway
E
REACTOME_CLASS_I_MHC_MEDIATED_ANTIGEN_PROCESSING_PRESENTATION
P < 0.001
NES = -1.20
REACTOME_ANTIGEN_PRESENTATION_FOLDING_ASSEMBLY_AND_PEPTIDE_LOADING_OF_CLASS_I_MHC
P = 0.019
NES = -1.30
Enrichment score
Rank
F
H2-Q1
H2-Q2
H2-Q4
H2-T3
Fraction of cells in group (%)
Mean Expression in group

Figure 5

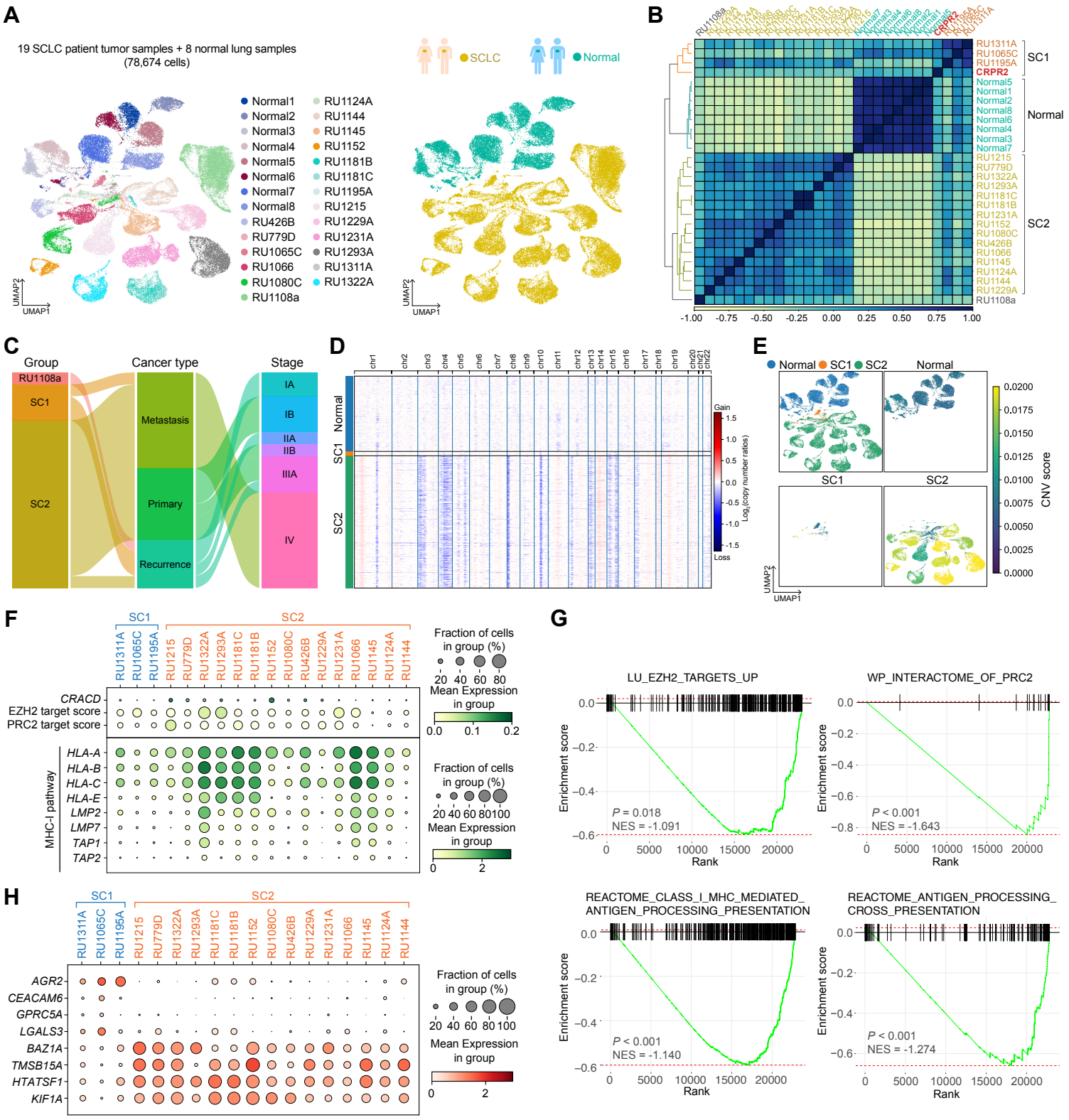
A
19 SCLC patient tumor samples + 8 normal lung samples
(78,674 cells)
SCLC
Normal
Normal1
Normal2
Normal3
Normal4
Normal5
Normal6
Normal7
Normal8
RU426B
RU779D
RU1065C
RU1066
RU1080C
RU1108a
RU1124A
RU1144
RU1145
RU1152
RU1181B
RU1181C
RU1195A
RU1215
RU1229A
RU1231A
RU1293A
RU1311A
RU1322A
UMAP1
UMAP2
B
SC1
Normal
SC2
CRPR2
C
Group
Cancer type
Stage
RU1108a
SC1
SC2
Metastasis
Primary
Recurrence
IA
IB
IIA
IIB
IIIA
IV
D
Normal
SC1
SC2
Gain
Loss
Log2(copy number ratios)
E
Normal
SC1
SC2
CNV score
F
Fraction of cells in group (%)
Mean Expression in group
CRACD
EZH2 target score
PRC2 target score
MHC-I pathway
HLA-A
HLA-B
HLA-C
HLA-E
LMP2
LMP7
TAP1
TAP2
G
LU_EZH2_TARGETS_UP
WP_INTERACTOME_OF_PRC2
REACTOME_CLASS_I_MHC_MEDIATED_ANTIGEN_PROCESSING_PRESENTATION
REACTOME_ANTIGEN_PROCESSING_CROSS_PRESENTATION
Enrichment score
Rank
P = 0.018
NES = -1.091
P < 0.001
NES = -1.643
P < 0.001
NES = -1.140
P < 0.001
NES = -1.274
H
AGR2
CEACAM6
GPRC5A
LGALS3
BAZ1A
TMSB15A
HTATSF1
KIF1A